PAPER • OPEN ACCESS

Graphene FETs with high and low mobilities have universal temperature-dependent properties

To cite this article: Jonathan H Gosling *et al* 2023 *Nanotechnology* **34** 125702

View the article online for updates and enhancements.

Graphene FETs with high and low mobilities have universal temperature-dependent properties

Jonathan H Gosling[1,2], Sergey V Morozov[3], Evgenii E Vdovin[3],
Mark T Greenaway[4], Yurii N Khanin[3], Zakhar Kudrynskyi[1],
Amalia Patanè[1], Laurence Eaves[1], Lyudmila Turyanska[2],
T Mark Fromhold[1] and Oleg Makarovsky[1,*]

[1] School of Physics and Astronomy, University of Nottingham, Nottingham, NG7 2RD, United Kingdom
[2] Centre for Additive Manufacturing, Faculty of Engineering, University of Nottingham, Nottingham, NG7 2RD, United Kingdom
[3] Institute of Microelectronics Technology RAS, Chernogolovka 142432, Russia
[4] Department of Physics, Loughborough University, Loughborough, LE11 3TU, United Kingdom

E-mail: Oleg.Makarovsky@nottingham.ac.uk

CrossMark

Abstract
We use phenomenological modelling and detailed experimental studies of charge carrier transport to investigate the dependence of the electrical resistivity, ρ, on gate voltage, V_g, for a series of monolayer graphene field effect transistors with mobilities, μ, ranging between 5000 and 250 000 cm^2 V^{-1} s^{-1} at low-temperature. Our measurements over a wide range of temperatures from 4 to 400 K can be fitted by the universal relation $\mu = 4/e\delta n_{\max}$ for all devices, where $\rho_{\max}$ is the resistivity maximum at the neutrality point and δn is an 'uncertainty' in the bipolar carrier density, given by the full width at half maximum of the resistivity peak expressed in terms of carrier density, n. This relation is consistent with thermal broadening of the carrier distribution and the presence of the disordered potential landscape consisting of so-called electron–hole puddles near the Dirac point. To demonstrate its utility, we combine this relation with temperature-dependent linearised Boltzmann transport calculations that include the effect of optical phonon scattering. This approach demonstrates the similarity in the temperature-dependent behaviour of carriers in different types of single layer graphene transistors with widely differing carrier mobilities. It can also account for the relative stability, over a wide temperature range, of the measured carrier mobility of each device.

Supplementary material for this article is available online

Keywords: graphene, convolution model, charged impurities, electrical properties

(Some figures may appear in colour only in the online journal)

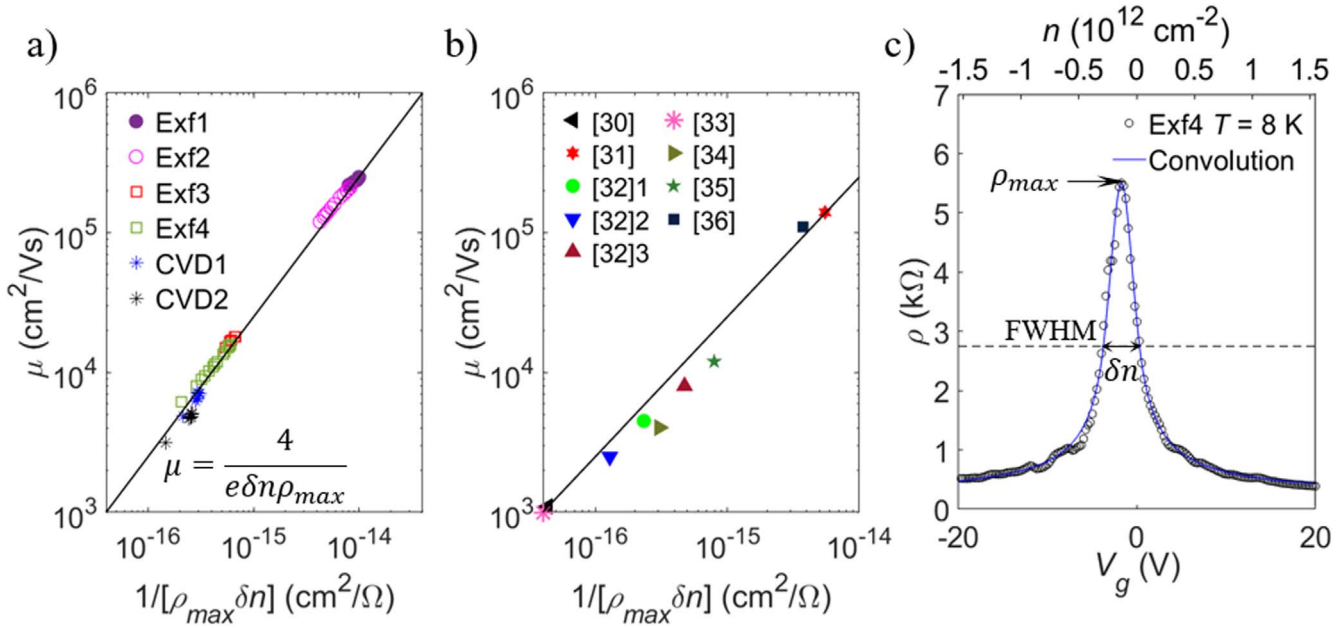* Author to whom any correspondence should be addressed.

1. Introduction

The electronic properties of a graphene-based field effect transistor (FET) are sensitive not only to the quality of the graphene layer but also to the way in which the device is fabricated. The very first graphene FETs had room temperature carrier mobilities of up to $\sim$10 000 cm^2 V^{-1} s^{-1} and

Figure 1. (a) Universal relation of the dependence of graphene mobility as a function of $1/(\delta n\, \rho_{max})$ for all the devices (see supplementary information SI1 for the sample details) over the wide temperature range (4 K $< T <$ 400 K) considered in this work, plotted as a series of data points for each device. The mobility has been calculated using the $\sigma(V_g)$ linearization technique[3] and verified by three other methods discussed later in the text (see supplementary information SI3 for details). (b) the same fit compared to graphene mobilities of other devices reported in [31–37]. (c) $\rho(V_g)$ curve for sample Exf4 at $T = 8$ K (data points) fitted by the convolution model (blue line) [38]. Details of the convolution model can be found in the supplementary information, SI2. Arrows indicate values of ρ_{max} and δn.

peak resistivities at the Dirac point of $\sim h/4e^2$ [1, 2]. More recently, low temperature mobilities well in excess of 100 000 cm^2 V^{-1} s^{-1} have been achieved by sandwiching a monolayer of exfoliated graphene between two layers of hexagonal boron nitride [3–5]. This has provided opportunities to observe novel physics and has significantly extended the temperature range of well-established quantum phenomena, e.g. the quantum Hall effect [6–8], magnetic flux-quantised Brown-Zak magneto-oscillations [9, 10], non-locality [5, 11] and magnetophonon resonance [12, 13]. Numerous phonon modes, namely acoustic and optical phonons [14–16], surface optical phonons in polar substrate materials [17–19] and flexural phonons [20] have been reported to have a strong impact on the temperature dependence of graphene's mobility. Extensive research has focused on upscaling the size of graphene layers by molecular beam epitaxy [11, 21], chemical vapour deposition, CVD [22, 23], thermal growth on silicon carbide [24, 25] or by inkjet-printing [26, 27]. It is widely acknowledged that the dominant scattering mechanism can differ in different graphene devices, ranging from those with ballistic transport [4, 5] to those with high impurity concentrations [28], and a number of models have been developed to characterise these devices. However, to date there is no model capable of explaining the temperature dependence of transport properties across all graphene FETs from high to low mobility.

Here, we investigate the electron transport properties of six different graphene FETs with low temperature mobilities ranging from 5000 cm^2 V^{-1} s^{-1} to 200 000 cm^2 V^{-1} s^{-1}. Despite this great disparity, the temperature dependence of their transport properties can all be fitted accurately using the

following universal relation with a small number (two) of easily measurable parameters: $\mu = 4/e\delta n\rho_{max}$, as shown in figures 1(a)–(b). In this equation, μ is the carrier mobility, ρ_{max} is the peak resistivity at the neutrality point, and δn is an 'uncertainty' in the bipolar carrier density, given by the full width at half maximum (FWHM) of the resistivity peak expressed in terms of carrier density. This 'uncertainty', δn, can be attributed to the presence of electron–hole puddles over the graphene plane [29], or to the uncertainty in electron energy in ballistic samples without such spatial disorder [30].

2. Methods

Our 6 SLG FETs can be divided into 3 groups according to their mobility (see table 1 and supplementary information SI1). The high mobility devices Exf1 and Exf2 ($\mu >$ 200 000 cm^2 V^{-1} s^{-1} at $T <$ 10 K) were fabricated using dry transfer of single layer graphene encapsulated between two hBN layers and dry-transfer onto a Si/SiO$_2$ substrate [4, 5, 39, 40]. The lower mobility devices Exf3 and Exf4 (10 000 $< \mu <$ 20 000 cm^2 V^{-1} s^{-1} at $T <$ 10 K) were fabricated using exfoliated SLG and conventional wet-transfer of graphene onto Si/SiO$_2$ [41] but without use of additional protective layers of hBN or other materials. The lowest mobility devices CVD1 and CVD2 ($\mu <$ 10 000 cm^2 V^{-1} s^{-1} at $T <$ 10 K) were fabricated using commercial CVD-hBN film heterostructures on SiO$_2$/Si wafers [42]. CVD2 was fabricated by capping half of the graphene layer of CVD1 with a thin ($\sim$1 μm) layer of exfoliated

Table 1. Sample details at $T < 10K$. The doping level ranging from 4×10^9 to 1.1×10^{12} cm^{-2} is derived from the position of the maximum resistivity relative to gate-induced doping.

Sample name	Processing technique	Dielectric layer width(nm)	Device length (μm)	Device width (μm)	Doping level (cm^{-2})	Measured mobility (cm^2 V^{-1} s^{-1})
Exf1	Dry transfer exfoliated	323	4	1	5.6×10^9	250 000
Exf2	Dry transfer exfoliated	308	4	4	4.1×10^9	210 000
Exf3	Wet transfer exfoliated	290	4	1	2.9×10^{10}	18 000
Exf4	Wet transfer exfoliated	290	4	1	3.0×10^{10}	16 000
CVD1	CVD	285	5	3	8.4×10^{11}	7000
CVD2	CVD	285	5	3	1.1×10^{12}	5000
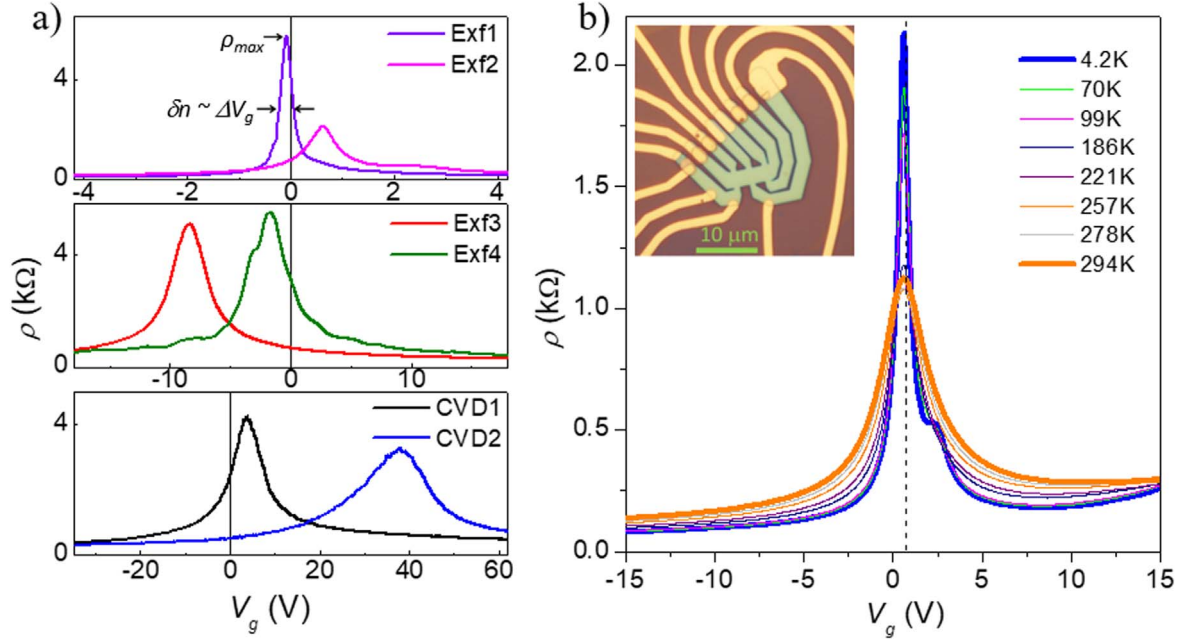
Figure 2. (a) Dependence of the resistivity on gate voltage, $\rho(V_g)$, at temperature $T \approx 5$ K for the six studied devices. δn is calculated from the full width at half maximum, FWHM (ΔV_g) of the $\rho(V_g)$ plot as $\delta n = \frac{C_A}{e} \Delta V_g$. (b) The $\rho(V_g)$ dependence for the high mobility exfoliated graphene device Exf2 measured at different temperatures. We attribute the asymmetric feature at $V_g \sim +3$ V at low temperatures to a local inhomogeneity or contact effects. The vertical dashed line indicates the position of the charge neutrality point. Inset: an optical image of this device with a 10 μm scale bar.

monocrystalline InSe using the technique described in [43]. We include the InSe/Graphene/SiO$_2$/Si device as an example of a more complex heterostructure where our model can be used. In surface-decorated graphene devices, the deposition of the top layer (InSe in this case) results in two key effects: (i) surface doping, as observed from the shift of the Fermi energy with respect to the Dirac point; (ii) the change of mobility due to additional scattering mechanisms related to the presence of donors in the InSe layer (in addition to acceptors present in SiO$_2$/Si). This behaviour is evident from the change of the slope of the $\rho(V_g)$ dependences and is confirmed by Hall measurements [43].

All six SLG films with doping level from $<10^{10}$ cm^{-2} to $>10^{12}$ cm^{-2} were processed into Hall bars of similar dimensions (a few microns) using electron beam lithography and Ti/Au contacts (see figure 2(b) and table 1). Their transport properties were measured in a helium-filled cryostat over a temperature range between $T = 4$ K and 400 K and at magnetic fields, B, up to 16 T using the 4-terminal measurement technique and high impedance voltmeters, hence significantly reducing contact resistance effects. The gate voltage (V_g) dependences of the measured Shubnikov–de Haas oscillations were used to determine the carrier sheet density [1] and hence the effective thickness of the insulating dielectric substrate, d, see table 1. These measurements enabled us to calculate the carrier concentration *versus* the applied gate voltage according to the relation $n = n_0 + C_A V_g/e$, where C_A is the effective areal gate capacitance, $C_A = \varepsilon \varepsilon_0/d$, and $n_0 = n(V_g = 0)$ is the carrier density due to unintentional doping (see table 1).

3. Results and discussion

3.1. Experimental data and universal temperature dependence of mobility

Figure 2(a) shows the $\rho(V_g)$ plots measured for each device. In the high mobility devices (Exf1 and Exf2) the Dirac (charge neutrality) point is at a low gate voltage (<1 V), corresponding to a low unintentional background doping level (n- or p-type $< \pm 10^{10}$ cm^{-2}). The lower mobility, Exf3, Exf4, CVD1 and CVD2, devices have p-type carrier concentrations, $p > 10^{10}$ cm^{-2} at $V_g = 0$, typical of CVD graphene FETs [44, 45]. The temperature dependence of the electrical properties of each device was measured over a wide range of gate voltages. An example is shown in figure 2(b) for the high mobility Exf2 device. The $\rho(V_g)$ curve is rather symmetric with respect of the Dirac point (dashed line in figure 2(b)), except of a feature observed at $V_g \sim +3$ V at low temperatures. We attribute this asymmetric feature to a local inhomogeneity or contact effects that are known to affect conductivity of small graphene channels, particularly in the ballistic regime, which was reported for similar graphene layers at temperatures as high as >200 K [4, 5].

In order to validate our 3-point method to extract the field-effect mobility from experimental measurements (figure 1), we compare our results with 4 other reported methods used for this analysis (see supplementary information SI3 for details): (i) fit of $\rho(V_g)$ measured at different temperatures using a convolution of linear conductivity $\sigma(n)$ and running box average δn [38], (figure 1(c)); (ii) linear fit of

$\sigma(V_g)$ at selected values of V_g where the slope of $\sigma(V_g)$ reaches its maximum; (iii) linearization of the whole $\sigma(V_g)$ curve taking into account the contribution of short range scattering resistivity, ρ_s [3]; (iv) from the maximum value of $d\sigma/dV_g$ [46]. For example for sample Exf4 at $T = 8$ K we obtained 15 000 cm^2 V^{-1} s^{-1} < μ < 16 000 cm^2 V^{-1} s^{-1} for all four methods, which is within a 10% error (figure 1(c) and supplementary information SI3 for other samples and temperatures). Methods (ii)–(iv) are widely used in the literature [3, 46] to calculate field effect mobility in graphene FETs (GFETs) at different temperatures. In general, all these methods analyse the slope of $\sigma(V_g)$ at V_g where it has maximum. Here, we show that the maximum value of μ is always measured in the vicinity of the FWHM points of the $R(V_g)$ curve. Thus, the region of gate voltages near the FWHM points of $R(V_g)$ is particularly important for the characterisation of GFETs since for all other gate voltages the mobility is lower. The decrease of μ in the vicinity of the Dirac point, inside the $|n| < \delta n/2$ region, is discussed later in the text. The decrease of μ at large V_g outside the $|n| < \delta n/2$ region can be treated using the linearization of $\sigma(V_g)$ and was discussed in [3]. Note that the maximum mobility considered in this work can be several times higher than the mobility at high carriers densities, far from the FWHM $R(V_g)$ region of carrier concentrations. The modelling of the electron conductivity and mobility in these devices require additional parameters, such as additional n-independent resistivity ρ_s arising from the presence of short-range scatterers [3].

Despite the apparent difference in the resistivity and its temperature dependence for each device (see figure 2), the measured mobility data for all six devices obey the following relation

$$\mu = \frac{4}{e \delta n \rho_{\text{max}}} \qquad (1)$$

as shown in figure 1(a). This simple relation can be derived from the $\rho(V_g)$ curve (see supplementary information, SI2) [38]. At the FWHM points of $\rho(V_g)$, $\sigma = \dfrac{2}{\rho_{\text{max}}}$ and $n = \dfrac{\delta n}{2}$. Therefore, using the relation $\sigma = en\mu$, we obtain equation (1). Figure 1(a) shows that equation (1) agrees well with the experimental data acquired over the temperature range 4 K < T < 400 K for the six devices. Our analysis of the experimental data also shows that this value of mobility is in good agreement with the field-effect mobility calculated by other methods: namely the linearisation of $\sigma(V_g)$ [3] and the value of mobility at the maximum of $d\sigma/dV_g$ (supplementary information, SI3).

Therefore, from the measured $\rho(V_g)$ curve of a graphene FET and using equation (1), we are able to derive the mobility. This way of calculating the field-effect mobility requires measurements of $\rho(V_g)$ at just 3 points (the 3-point method): one at $\rho(V_g) = \rho_{\text{max}}$ and two at the FWHM points, with $\rho(V_g) = \rho_{\text{max}}/2$. This 3-point method provides a better defined estimate of the field-effect mobility in the vicinity of the Dirac point, $|n| < \delta n/2$, compared to the method of linearisation of $\sigma(V_g)$. In particular, it is well defined even if $\sigma(V_g)$ has a nonlinear dependence, as for the case of strong

short range scattering [3] (see supplementary SI3). Here we assume electron–hole symmetry of carrier transport in the vicinity of the Dirac point, $|n| < \delta n/2$, resulting in the symmetric $R(V_g)$ curves (figure 1(c)). In some cases $R(V_g)$ can be asymmetric, resulting in an uncertainty of carrier (electron and hole) mobility. To date there is no single model to explain this asymmetry, with the majority of studies suggesting an increased asymmetry could be related to an increasing number of charged impurities [47–49]. We found a small number of graphene FET types where the 3-point mobility has large uncertainty. These include devices where a simple parallel plate capacitance model does not work, such as graphene FETs with a large number of traps that charge/discharge slowly, such as graphene/perovskite heterostructures. In this case, the specific form of the $R(V_g)$ curve depends on a number of parameters such as the V_g sweep rate and its direction [50]. Also, this model cannot account for flake-to-flake resistance in disordered inkjet-printed graphene networks [27, 51], investigated e.g. for flexible electronics. The low mobility of these networks and differences in the network organization require further studies.

Equation (1), which fits our measured data for all six devices over a wide range of temperatures, can be expressed in a different form by considering the motion of a single electron at the Fermi energy. As used in the weak localisation theory of graphene [52], the Drude model provides the following expression for the mobility, $\mu = el/v_F m^*$, where $l = v_F \tau$ is the carrier mean free path, τ is its scattering time, and $m^* = \hbar k_F / v_F$. The carrier wavevector is given by the relation $k_F^2 = \pi n$, so that the uncertainty in the wavevector at the Fermi energy is $\delta k_F = \pi \delta n / 2 k_F$. Combining these expressions, equation (1) takes the form

$$l \delta k_F = \frac{R_Q}{\rho_{\text{max}}}, \qquad (2)$$

where $R_Q = h/e^2 \approx 25.8$ kΩ is the quantum of resistance. For our six devices, ρ_{max} ranges between ∼2 and 6 kΩ. Therefore $l \delta k_F$ is well in excess of unity, in analogy with the wave uncertainty relation, $\Delta x \Delta k > 1/2$. We note that a significantly higher value of $\rho_{\text{max}} \sim 19$ kΩ at 5 K was measured for high mobility suspended graphene [20]. In this case $l \delta k_F \tilde{} 0.7$. A relation based on the Landauer formalism for ballistic electron transport in monolayer and bilayer graphene and the time-energy uncertainty principle, which is similar to equation (2), was obtained by Dragoman [30], who argued that the peak resistivity of graphene was equal to $R_Q/4$.

3.2. Analytical model of T-dependent transport properties

Our phenomenological model from which equation (1) is derived, provides a good fit to the temperature-dependent mobility using two experimentally measured parameters: ρ_{max} and δn. We propose that, since the value of δn is experimentally derived and describes the broadening near the Dirac point, it accounts for the doping level and the effect of different scattering mechanisms, including different phonons, substrate imperfections, etc. This makes our approach different from previously presented graphene mobility and
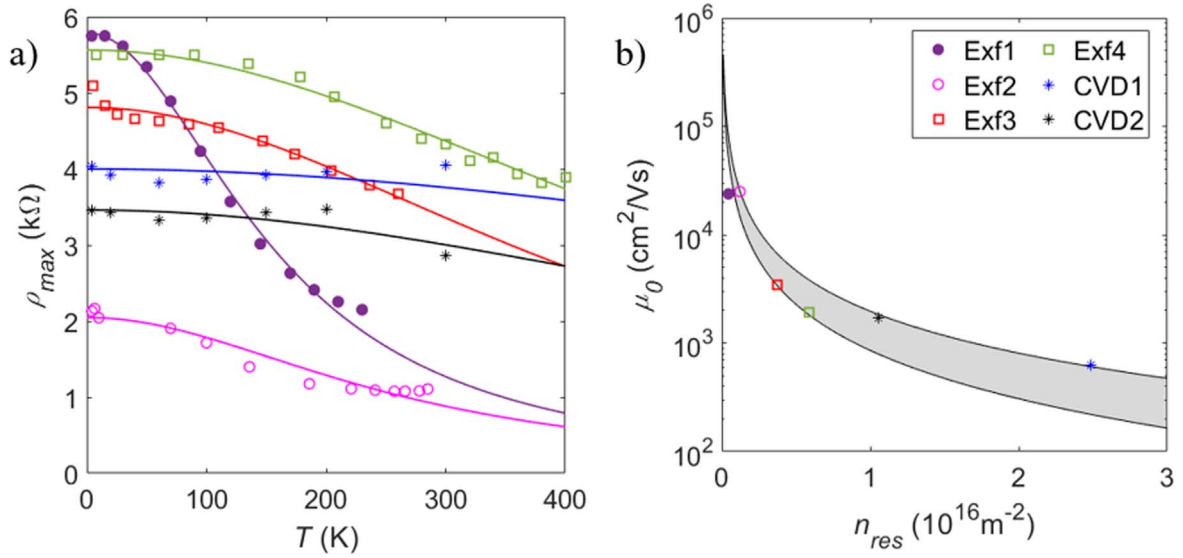
Figure 3. (a) Maximum resistivity, $\rho_{\max}$, as function of temperature for all 6 devices as shown by the data points, see legend in (b). The solid lines are determined using equation (4). (b) The parameters μ_0, mobility at the charge neutrality point, and n_{res}, residual carrier density at charge neutrality, used in (a) for each device are compared to the model reported in [53] within a range of impurity stand-off distances, 0.3 nm $\lesssim d_{\mathrm{imp}} \lesssim$ 1 nm (grey shaded region).

conductivity models based on a number of parameters with large experimental uncertainty, such as distance to charge impurities [53] or different graphene and substrate phonon energies [16–18].

To model $\mu(T)$ in more detail, we first consider the effect of temperature on $\rho_{\max}$ and δn. Since δn represents an uncertainty in the charge density near the Dirac point and $\rho_{\max}$ is directly related to δn, they both involve temperature-induced broadening described by the Fermi–Dirac (FD) function [1]. The minimum carrier density at the neutrality (Dirac) point is $n_{\mathrm{NP}} = n_{\mathrm{res}} + n_{\mathrm{TH}}$, where n_{res} is the sheet density of the residual carriers due to spatial variations of the potential landscape caused by, for example, charged impurities or surface corrugations [53] and

$$n_{\mathrm{TH}} = \frac{\pi}{3}\left(\frac{k_{\mathrm{B}}T}{\hbar v_{\mathrm{F}}}\right)^2, \tag{3}$$

is the density of thermally activated electron–hole pairs determined by the FD distribution function (see supplementary information SI4). Therefore

$$\rho_{\max} = \frac{1}{e\mu_0 n_{NP}} = \frac{1}{e\mu_0(n_{res} + n_{TH}(T))}, \tag{4}$$

where μ_0 is the mobility at the Dirac point. Since phonon scattering is expected to be relatively weak around the Dirac point [54], we make the approximation that μ_0 is temperature-independent.

Equation (4) provides a good fit to the measured values of $\rho_{\max}(T)$ for all six devices using μ_0 and n_{res} as fitting parameters, see figure 3(a). The average deviation of our model from the data is less than 10% for all devices [55]. The values of the fitting parameters for each sample are shown as a plot of μ_0 versus n_{res} in figure 3(b). Their values are consistent with those obtained using a model [53] for graphene on SiO$_2$, with the average separation, d_{imp}, between the

impurities and the graphene layer within a range of 0.3 nm $\lesssim$ $d_{\mathrm{imp}} \lesssim$ 1 nm (see grey shaded region in figure 3(b)). The relatively large value of $\rho_{\max}$ observed for Exf1 at low temperatures may be partly related to the ballistic motion of carriers previously reported for similar devices [4, 5]. At low temperatures, the maximum resistivity of pristine high mobility graphene films can be defined using quantum conductance units as $\rho_{\max}(T) = h/4e^2 \approx 6$ kΩ [2].

Substituting equation (4) into equation (1), we obtain the following expression

$$\delta n = 4n_{\mathrm{NP}}(\mu_0/\mu), \tag{5}$$

where μ_0 is the mobility at the Dirac point and μ is the mobility defined by equation (1), i.e. at the half-maximum point of the resistivity. This expression indicates that δn is proportional to the total carrier density at the Dirac point and also proportional to the ratio of the mobility at the Dirac point to that at the half maximum. Assuming that the mobility is constant, $\mu_0 = \mu$, equation (5) becomes $\delta n(T) = 4n_{\mathrm{NP}}(T)$. The resulting T-dependence of δn is shown by the dashed lines in figure 4(a) for the different values of n_{res} given in the figure caption. For the low mobility devices, we find that the effect of residual charge is particularly important, resulting in the non-zero δn at low temperatures where $\delta n \approx 4n_{\mathrm{res}}$. The residual sheet density, n_{res}, is also responsible in part for the low mobility measured for the CVD devices [53], for which we found that $\delta n \approx n_{\mathrm{imp}}$ [38], For the hypothetical case when n_{res} = 0 (no charged impurities, no e–h puddles, etc), the FWHM would be dependant only on the thermally excited carrier density, n_{TH}, given by equation (3), and has no fitting parameters (see the bold dashed line in figure 4(a) starting from the $\delta n = T = 0$ origin). This model provides good qualitative agreement with the measured $\delta n(T)$ for the low mobility devices and at low temperatures, $T < 100$ K. However, at high temperature we find a weaker increase in $\delta n(T)$ than the
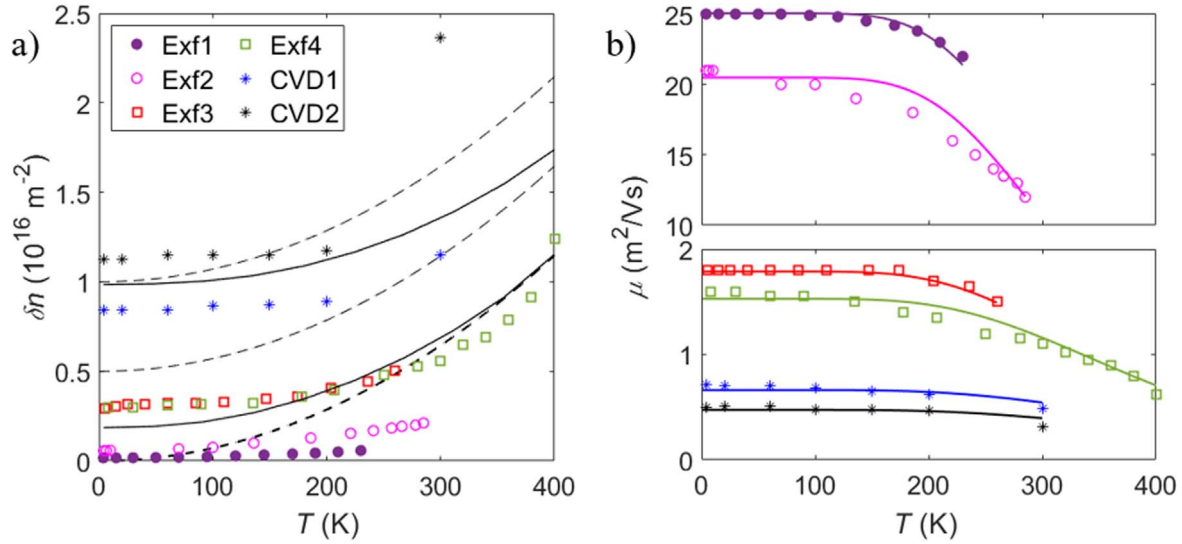
Figure 4. (a) Temperature dependence of the 'uncertainty' of carrier concentration, δn. The data points are the measured $\delta n(T)$ dependences for the 6 devices; dashed lines: results of the Fermi–Dirac model with $\delta n = 4(n_{res} + n_{TH})$ and $n_{res} = 0$, 1.25×10^{15} and 2.5×10^{15} m^{-2} (see equation (3)); solid lines: results using conductivity calculations including substrate impurities and phonons, see text and supplementary information, SI5 for details. (b) Mobility, μ, calculated at the half maximum resistivity using equation (8) as a function of temperature for all devices (solid lines), compared to the experimentally measured mobility (data points).

one predicted by the relation $\delta n(T) = 4[n_{res} + n_{TH}(T)]$. This suggests that the electron mobility varies significantly in the vicinity of the Dirac point $|n| < \delta n/2$, i.e. $\mu_0/\mu < 1$ in equation (5). By modelling the substrate scattering effects (charged impurities and substrate phonons) at a finite distance from the graphene plane, we find that $\mu_0/\mu < 1$ (see Supplementary Information, SI5 and figure S7(b)). These results, which are included in figure 4(a) as solid lines, are in better agreement with the measurements.

The measurements of the high mobility devices, in particular Exf1, reveal a weak $\delta n(T)$ dependence (figure 4(a)), suggesting an even stronger relative decrease of mobility close to the Dirac point (supplementary information, figure S9c). Our initial assumption of a gate voltage-independent mobility cannot be applied to the high mobility devices ($>100\,000$ cm^2 V^{-1} s^{-1}) in the vicinity of the Dirac point. Unfortunately, experimental measurements of the Hall carrier concentration and mobility have a large uncertainty at gate voltages close to the Dirac point where $|n| < \delta n/2$, due to the presence of both electron and hole carriers. Given the very weak impurity scattering, we are unable to attribute this dependence of mobility on carrier density to substrate scattering effects in the high mobility samples. However, it is also known that high mobility quasi-ballistic devices are sensitive to the detailed electrostatics within the device and can be non-ohmic [56, 57]. Therefore, changes in the applied bias voltage dropped across the ballistic transport regions of high mobility devices can result in changes to the measured resistivity as has been shown theoretically [58] (see also supplementary information SI6). Nevertheless, the mobility calculated using equation (1) (figure 1(a)) and the convolution fit of the full $\rho(V_g)$ provides a good agreement with the measurements on the high mobility, quasi-ballistic devices, Exf1 and Exf2 (see figure S4) as well as low mobility devices, CVD1 and CVD2, characterised by the diffusive transport. Thus, we propose that

the phenomenological model presented by the equation (1) provides a bridge between the drift-diffusion and ballistic approach to the carrier mobility in graphene.

Now that we have established that the mobility calculated around the half-maximum of the charge density given by equation (5) agrees closely with the measured mobility, we can study the temperature dependence of the measured mobility, $\mu(T)$. To model the temperature dependence of mobility explicitly, decoupled from ρ_{max} and δn, it is necessary to include the influence of temperature-dependent scattering on the mobility, for which we use a linearised Boltzmann approach.

There exist several intrinsic phonon modes in graphene, as well as extrinsic substrate polarons, all of which have been reported to affect the conductivity of graphene under varying conditions [16, 17, 19]. To gain an insight into the nature of temperature-dependent electron scattering influencing the measured $\mu(T)$ relation in different samples, we simplify the effects of phonon scattering by fitting the data using a single optical phonon and an electron-phonon coupling strength that depends on the environment of each individual graphene sample.

We consider a single relaxation time, $\tau_{op}(\varepsilon, T)$, to model the optical phonon scattering, which has both a temperature and energy dependance given by [16]

$$\frac{1}{\tau_{op}(\varepsilon, T)} \propto \left[N(\omega_O, T)|\varepsilon + \hbar\omega_o| \frac{1 - f(\varepsilon + \hbar\omega_o, T)}{1 - f(\varepsilon, T)} + (N(\omega_o, T) + 1)|\varepsilon - \hbar\omega_o| \frac{1 - f(\varepsilon - \hbar\omega_o, T)}{1 - f(\varepsilon, T)} \right],$$

(6)

where $N(\omega_o, T)$ is the phonon occupation for frequency, ω_o, and temperature, T, and $|...|$ represents the modulus. We make the approximation $\mu \approx ev^2\tau(\varepsilon_F)/\varepsilon_F$, which is exact in

the limit $T \to 0$. For $\varepsilon_F < \hbar\omega_o$; the mobility is then given by

$$\frac{1}{\mu} = \frac{1}{\mu_c} + \frac{D_{op}\sqrt{\delta n/2}}{\sinh\left(\frac{\hbar\omega_0}{k_B T}\right)}. \quad (7)$$

Here, μ_c is the mobility in the low temperature limit and we have assumed that the carrier density varies as $n \propto \varepsilon_F^2$ (strictly true only in the limit $\varepsilon_F \gg k_B T$). In equation (7), D_{op}, is a constant related to the optical phonon gauge field coupling strength, β_{op}, given by $D_{op} = 2\beta_{op}^2\pi^{1/2}/(ev_F^3\rho_m)$, where ρ_m is the mass density of graphene. Substituting equation (5) for δn into equation (7) and solving the resulting self-consistent equation we obtain the following relation

$$\frac{\mu}{\mu_0} = D_{op}^2 \frac{\mu_c^2}{2} \frac{n_{NP}(T)}{\sinh^2\left(\frac{\hbar\omega_o}{k_B T}\right)} \left[1 - \sqrt{1 + \frac{2\sinh^2\left(\frac{\hbar\omega_o}{k_B T}\right)}{D_{op}^2\mu_c\mu_0 n_{NP}(T)}} \right]^2. \quad (8)$$

We have determined the values of n_{res} and μ_0 for each device from the measured ρ_{max} using equation (4), see figure 3. The two parameters determining the phonon contribution to mobility, D_{op} and ω_o, are determined through fitting to the measured data in figure 4(b). The phonon frequency, ω_o, determines the onset of phonon occupation, triggering the decrease in phonon-limited mobility. For simplicity, we use a single energy of $\hbar\omega_o = 100$ meV, to approximate the range of high energy optical phonon modes in graphene and neighbouring substrate materials (hBN, SiO_2) [16, 18, 59, 60]. The gives a significant onset of phonon occupation around $T \approx 200$ K, in qualitative agreement with the measured decrease of mobility decrease shown in figure 4(b). This approximates to the range of weakly dispersed, higher energy phonon modes of the gated graphene devices. The typical value of the gauge field strength for single optical phonons in graphene is $\beta_{op} \approx 12$ eV Å^{-1} [16], which gives an estimation of $D_{op} \approx 1 \times 10^{-8}$ V^{-1} s^{-1} m^{-1}. We find that a value of $D_{op} = 3 \times 10^{-8}$ V^{-1} s^{-1} m^{-1} provides a good fit for the high mobility exfoliated graphene on hBN, while $D_{op} = 1 \times 10^{-7}$ V^{-1} s^{-1} m^{-1} fits the lower mobility exfoliated devices with graphene on SiO_2 and the lowest mobility CVD devices (figure 4(b)). These values of D_{op} are larger than the estimated value deduced from the single optical gauge field strength since, for simplicity, we use a single energy, 100 meV, for the optical phonon modes with a single average scattering rate. We note that a discrepancy exists between the values of D_{op} for the different sets of devices. Although we do not consider in detail the full phonon spectrum of the various devices, the analysis provides an insight into the relative strength of phonon scattering in different samples. Differences between the environment of the different graphene samples, the surrounding materials, and even distances to the substrates, are likely to affect the details of polar and remote optical phonon scattering in each sample. Stronger substrate phonon scattering for graphene on SiO_2, which arises from the weaker screening and a lower energy onset of phonon occupancy

[59], likely results in different fitting parameters, D_{op}. For the high mobility samples, it is also likely that there still exist thermally excited carriers at the half maximum of resistivity, where $\varepsilon_F \sim k_B T$. In this case, the lower apparent strength of phonon scattering for the high mobility samples could compensate for the increased carrier density at high temperatures.

4. Conclusions

In summary, we have presented a phenomenological model to account for a universal temperature dependence of graphene's mobility, μ, based on a concept of a charge density uncertainty, δn, given by the full width half maximum of the maximum in resistivity at the Dirac point, and the relation $\rho_{max} = 4/e\mu\delta n$, as shown in figure 1. This relation is found to be accurate for all of the graphene layers including both exfoliated and CVD grown SLG devices which have electron mobilities ranging from 5000 to 250 000 cm^2 V^{-1} s^{-1} over the temperature range 4 K $< T <$ 400 K. It provides an expression that estimates the field effect mobility from $\rho(V_g)$, which requires only 3 experimental data points: $\rho(V_g) = \rho_{max}$ and the width of the resistivity peak $\rho(V_g) = \rho_{max}/2$, thus offering a simple method for analysing the experimental data in the vicinity of the Dirac point. Our model does not discriminate between and does not account for the contributions of different factors to the electrical conductivity, such as different possible scattering mechanisms, which require complex quantum mechanical studies. We also present an analytical model, based on scattering by charged impurities and phonons, that describes and interrelates the temperature dependences of each of the transport parameters: ρ_{max}, δn and μ. It demonstrates that the resistivity of graphene at low carrier concentrations, $n < \delta n$, which is typically excluded from the data analysis due to the nonlinear $\sigma(n)$, can be analysed using a model based on Fermi–Dirac temperature broadening and impurity-induced broadening of δn.

Data availability statement

The data that support the findings of this study are available upon reasonable request from the authors.

ORCID iDs

Sergey V Morozov ⓘ https://orcid.org/0000-0003-3075-7787
Evgenii E Vdovin ⓘ https://orcid.org/0000-0002-7501-3223
Mark T Greenaway ⓘ https://orcid.org/0000-0003-3243-3794
Amalia Patanè ⓘ https://orcid.org/0000-0003-3015-9496
Lyudmila Turyanska ⓘ https://orcid.org/0000-0002-9552-6501
Oleg Makarovsky ⓘ https://orcid.org/0000-0002-8625-5084

References

[1] Novoselov K S *et al* 2004 Electric field effect in atomically thin carbon films *Science* **306** 666–9

[2] Novoselov K S *et al* 2005 Two-dimensional gas of massless Dirac fermions in graphene *Nature* **438** 197–200

[3] Morozov S V *et al* 2008 Giant intrinsic carrier mobilities in graphene and its bilayer *Phys. Rev. Lett.* **100** 016602

[4] Mayorov A S *et al* 2011 Micrometer-scale ballistic transport in encapsulated graphene at room temperature *Nano Lett.* **11** 2396–9

[5] Abanin D A *et al* 2011 Giant nonlocality near the dirac point in graphene *Science* **332** 328–30

[6] Zhang Y B, Tan Y W, Stormer H L and Kim P 2005 Experimental observation of the quantum Hall effect and Berry's phase in graphene *Nature* **438** 201–4

[7] Novoselov K S *et al* 2007 Room-temperature quantum hall effect in graphene *Science* **315** 1379

[8] Tanaka M *et al* 2022 Temperature-induced phase transitions in the correlated quantum Hall state of bilayer graphene *Phys. Rev. B* **105** 075427

[9] Kumar R K *et al* 2017 High-temperature quantum oscillations caused by recurring Bloch states in graphene superlattices *Science* **357** 181–4

[10] Kumar R K *et al* 2018 High-order fractal states in graphene superlattices *PNAS* **115** 5135–9

[11] Moreau E *et al* 2010 Graphene growth by molecular beam epitaxy on the carbon-face of SiC *Appl. Phys. Lett.* **97** 241907

[12] Kumaravadivel P *et al* 2019 Strong magnetophonon oscillations in extra-large graphene *Nat. Commun.* **10** 3334

[13] Greenaway M T *et al* 2021 Graphene's non-equilibrium fermions reveal Doppler-shifted magnetophonon resonances accompanied by mach supersonic and Landau velocity effects *Nat. Commun.* **12** 6392

[14] Greenaway M T, Kumar R K, Kumaravadivel P, Geim A K and Eaves L 2019 Magnetophonon spectroscopy of dirac fermion scattering by transverse and longitudinal acoustic phonons in graphene *Phys. Rev. B* **100** 155120

[15] Piscanec S, Lazzeri M, Mauri F and Ferrari A C 2007 Optical phonons of graphene and nanotubes *Eur. Phys. J-Spec. Top* **148** 159–70

[16] Sohier T *et al* 2014 Phonon-limited resistivity of graphene by first-principles calculations: Electron-phonon interactions, strain-induced gauge field, and Boltzmann equation *Phys. Rev. B* **90** 125414

[17] Chen J H, Jang C, Xiao S D, Ishigami M and Fuhrer M S 2008 Intrinsic and extrinsic performance limits of graphene devices on SiO_2 *Nat. Nanotechnol.* **3** 206–9

[18] Dorgan V E, Bae M H and Pop E 2010 Mobility and saturation velocity in graphene on SiO_2 *Appl. Phys. Lett.* **97** 082112

[19] Konar A, Fang T A and Jena D 2010 Effect of high-kappa gate dielectrics on charge transport in graphene-based field effect transistors *Phys. Rev. B* **82** 115452

[20] Castro E V *et al* 2010 Limits on charge carrier mobility in suspended graphene due to flexural phonons *Phys. Rev. Lett.* **105** 266601

[21] Davies A *et al* 2018 Lattice-matched epitaxial graphene grown on boron nitride *Nano Lett.* **18** 498–504

[22] Reina A *et al* 2009 Large area, few-layer graphene films on arbitrary substrates by chemical vapor deposition *Nano Lett.* **9** 30–5

[23] Chen B Y *et al* 2014 How good can CVD-grown monolayer graphene be ? *Nanoscale* **6** 15255–61

[24] Berger C *et al* 2004 Ultrathin epitaxial graphite: 2D electron gas properties and a route toward graphene-based nanoelectronics *J. Phys. Chem. B* **108** 19912–6

[25] Huang J *et al* 2015 Physics of a disordered dirac point in epitaxial graphene from temperature-dependent magnetotransport measurements *Phys. Rev. B* **92** 075407

[26] Carey T *et al* 2017 Fully inkjet-printed two-dimensional material field-effect heterojunctions for wearable and textile electronics *Nat. Commun.* **8** 1202

[27] Wang F R *et al* 2021 Inter-flake quantum transport of electrons and holes in inkjet-printed graphene devices *Adv. Funct. Mater.* **31.5** 2007478

[28] Hwang E H and Das Sarma S 2009 Screening-induced temperature-dependent transport in two-dimensional graphene *Phys. Rev. B* **79** 165404

[29] Martin J *et al* 2008 Observation of electron–hole puddles in graphene using a scanning single-electron transistor *Nat. Phys.* **4** 144–8

[30] Dragoman D 2010 Low-energy conductivity of single- and double-layer graphene from the uncertainty principle *Phys. Scr.* **81** 035702

[31] Iacovella F *et al* 2014 Magneto-transport properties of a random distribution of few-layer graphene patches *J. Appl. Phys.* **116** 193705

[32] Wang L *et al* 2013 One-dimensional electrical contact to a two-dimensional material *Science* **342** 614–7

[33] Ponomarenko L A *et al* 2009 Effect of a high-kappa environment on charge carrier mobility in graphene *Phys. Rev. Lett.* **102** 206603

[34] Pezzini S, Cobaleda C, Diez E and Bellani V 2012 Quantum interference corrections to magnetoconductivity in graphene *Phys. Rev. B* **85** 165451

[35] Tikhonenko F V, Kozikov A A, Savchenko A K and Gorbachev R V 2009 Transition between electron localization and antilocalization in graphene *Phys. Rev. Lett.* **103** 226801

[36] Wang Z *et al* 2016 Origin and magnitude of 'designer' spin–orbit interaction in graphene on semiconducting transition metal dichalcogenides *Phys. Rev. X* **6** 041020

[37] Konstantatos G *et al* 2012 Hybrid graphene-quantum dot phototransistors with ultrahigh gain *Nat. Nanotechnol.* **7** 363–8

[38] Gosling J H *et al* 2021 universal mobility characteristics of graphene originating from charge scattering by ionised impurities *Commun. Phys.* **4** 1–8

[39] Kretinin A V *et al* 2014 Electronic properties of graphene encapsulated with different two-dimensional atomic crystals *Nano Lett.* **14** 3270–6

[40] Kinoshita K *et al* 2019 Dry release transfer of graphene and few-layer h-BN by utilizing thermoplasticity of polypropylene carbonate *Npj 2d Mater. Appl.* **3** 22

[41] Backes C *et al* 2020 Production and processing of graphene and related materials *2D Mater.* **7** 022001

[42] 2022 Monolayer graphene on 1cm x 1cm silicon wafers (p-doped) with a 285 nanometer silicon dioxide coating has been purchased from Graphene Supermarket (Graphene Laboratories Inc.)

[43] Kudrynskyi Z R *et al* 2017 Giant quantum hall plateau in graphene coupled to an inse van der waals crystal *Phys. Rev. Lett.* **119** 157701

[44] Sun Z Z *et al* 2010 Growth of graphene from solid carbon sources *Nature* **468** 549–52

[45] Tao L *et al* 2013 Inductively heated synthesized graphene with record transistor mobility on oxidized silicon substrates at room temperature *Appl. Phys. Lett.* **103** 183115

[46] Chen F, Xia J L and Tao N J 2009 Ionic Screening of Charged-Impurity Scattering in Graphene *Nano Lett.* **9** 1621–5

[47] Chen J H *et al* 2008 Charged-impurity scattering in graphene *Nat. Phys.* **4** 377–81

[48] Farmer D B *et al* 2009 Chemical doping and electron–hole conduction asymmetry in graphene devices *Nano Lett.* **9** 388–92

[49] Li J Y *et al* 2017 Electron hole symmetry breaking in charge transport in nitrogen-doped graphene *Acs Nano* **11** 4641–50

[50] Cottam N D *et al* 2020 Defect-assisted high photoconductive UV–visible gain in perovskite-decorated graphene transistors *Acs Appl. Electron. Mater.* **2** 147–54

[51] Barwich S *et al* 2021 On the relationship between morphology and conductivity in nanosheet networks *Carbon* **171** 306–19

[52] Tikhonenko F V, Horsell D W, Gorbachev R V and Savchenko A K 2008 Weak localization in graphene flakes *Phys. Rev. Lett.* **100** 056802

[53] Adam S, Hwang E H, Galitski V M, Sarma D and A S 2007 self-consistent theory for graphene transport *PNAS* **104** 18392–7

[54] Das Sarma S, Adam S, Hwang E H and Rossi E 2011 Electronic transport in two-dimensional graphene *Rev. Mod. Phys.* **83** 407–70

[55] 2022 Method of least squares used to find optimal values, nres and μ. For CVD1 device, the optimal solution is nres → ∞ and μ → 0. We restricted nres < 2.5×10^{16} m^{-2}, where we find the optimal solution fits within the bounds of 0.3 nm $\lesssim$ d $\lesssim$ 1 nm (grey shaded region in figure 3b) and remains well within a 10% deviation of the data

[56] Rahman S F A, Kasai S and Hashim A M 2012 Room temperature nonlinear operation of a graphene-based three-branch nanojunction device with chemical doping *Appl. Phys. Lett.* **100** 193116

[57] Boland M J, Sundararajan A, Farrokhi M J and Strachan D R 2016 Nonlinear ballistic transport in an atomically thin material *Acs Nano* **10** 1231–9

[58] Vandecasteele N, Barreiro A, Lazzeri M, Bachtold A and Mauri F 2010 Current–voltage characteristics of graphene devices: interplay between zener-klein tunneling and defects *Phys. Rev.* B **82** 045416

[59] Schiefele J, Sols F and Guinea F 2012 Temperature dependence of the conductivity of graphene on boron nitride *Phys. Rev.* B **85** 195420

[60] Vdovin E E *et al* 2016 Phonon-assisted resonant tunneling of electrons in graphene-boron nitride transistors *Phys. Rev. Lett.* **116** 186603